Received: 2 December 2020 | Revised: 1 November 2021 | Accepted: 16 November 2021

DOI: 10.1002/er.7518

RESEARCH ARTICLE

INTERNATIONAL JOURNAL OF ENERGY RESEARCH WILEY

Total solar spectrum energy converter with integrated photovoltaics, thermoelectrics, and thermal energy storage: System modeling and design

Nicholas Farrar-Foley | **Nicolas Augustus Rongione** | **Huan Wu** | **Adrienne S. Lavine** | **Yongjie Hu**

Department of Mechanical and Aerospace Engineering, University of California, Los Angeles, California, USA

Correspondence
Adrienne S. Lavine, Department of Mechanical and Aerospace Engineering, University of California, Los Angeles, CA 90095, USA.
Email: lavine@seas.ucla.edu

Funding information
American Chemical Society Petroleum Research Fund, Grant/Award Number: 58206-DNI5; Anthony and Jeanne Pritzker Family Foundation; National Science Foundation, Grant/Award Numbers: CAREER Award under Grant DMR-1753393, Graduate Research Fellowship under Grant 15-597; Sustainable LA Grand Challenge; U.S. Air Force Office of Scientific Research, Grant/Award Number: Young Investigator Award Grant FA9550-17-1-0149

Summary

A total-spectrum-utilizing integrated photovoltaic (PV), thermoelectric (TEG), and thermal energy storage fluid (TES) solar energy converter (PV-TEG-TES) with novel device architecture is proposed, and its performance is modeled to demonstrate its viability and optimize its system-level design. By incorporating a top-layer GaAs PV, ultraviolet and visible light is absorbed and converted directly to electricity, while infrared radiation passes through the PV. This infrared radiation is then captured by the TEG and TES layers to supply additional electricity or to be stored as thermal energy. In addition, the TEG converts to electricity otherwise wasted heat from thermalization of photons within the PV layer, and the TES effectively cools the PV, keeping it within adequate operating temperatures. According to analysis predicting upper bound performance, this PV-TEG-TES device can outperform the electrical conversion efficiency of a single GaAs solar cell module by 1.9 percentage points (from 24.1% for PV alone to 26.0% for the combined device, a relative 7.9% improvement), and can convert and store a total of 79.3% of incident solar energy under a concentration ratio of 673 suns per direct solar spectrum. An analytical framework using a successive overrelaxation technique for solutions to the nonlinearly coupled radiative, thermal, fluid, and electrical phenomena in such a PV-TEG-TES device is also discussed, offering a starting point for practical device parameters.

KEYWORDS

energy efficiency, full spectrum, gallium arsenide, hybrid solar-thermal energy conversion, solar energy, solar cell

1 | INTRODUCTION

1.1 | Device motivation

Global energy use is an increasingly crucial concern due to its resulting environmental and geopolitical issues. To mitigate these issues, development of clean, safe, and sustainable energy resources is in great demand, prompting much exploration of solar energy harvesting technologies. The two most common solar-electric power conversion technologies—photovoltaic solar cells (PV) and concentrating solar thermal power

(CSP)—each have unique advantages and disadvantages. Individual PV panels utilize only a fraction of the solar spectrum, resulting in relatively low conversion efficiency; for comparison, the best monocrystalline-based solar cells on the market today are around 22% efficient.[1] Solar spectrum utilization is increased using stacked "multijunction" solar cells with progressively lower band gaps, which have been shown to be up to 47% efficient,[2] but this layering increases material, fabrication, and ultimately module costs, and may make these modules prohibitively expensive.[3] In addition, PV cells alone lack inherent energy storage capability, prohibiting electricity production while not illuminated (during cloud cover, night, etc.). Concentrating mirrors or lenses have been implemented to reduce the amount of expensive semiconductor material used in highly efficient multijunction cells, thereby reducing the ratio of cost to power. However, concentration leads to high heat dissipation in the cells, degrading their performance and leaving much energy wasted in the form of heat.

Concentrating solar thermal power technologies focus and convert sunlight to heat, using a heat engine to convert this thermal energy to electricity, generally through Rankine[4,5] or Brayton cycles.[6] Unlike most PV, CSP thus has the capability to capture the entire solar spectrum, but due to high upfront and infrastructure costs CSP is generally a less economically viable option.[7] Further, CSP often incorporates inherent (thermal) energy storage which can be dispatched when the sun is not shining, a time coinciding with peak electricity demand.[8] Overall, CSP suffers from relatively low solar-electrical conversion efficiency, and high costs. New PV and CSP designs are thus required to meet the industry demand.

Though a far less ubiquitous form of energy conversion, the development of thermoelectric materials and generators has been advancing rapidly in recent years and could offer solid-state, maintenance-free, reliable power generation from waste heat sources.[9-12] Thermoelectric generators (TEG) typically consist of pellets of n- and p-type doped material connected electrically in series and thermally in parallel, whereby increasing the number of pellet pairs, the operating voltage of such a device can be increased. Exploring hybrid solar-thermoelectric energy generation systems (STEGs) is not a new concept.[13-15] For solar energy conversion, STEGs are often utilized in conjunction with PV or concentrators are applied. The inherently low efficiencies of STEGs compared to PV limit their lone use in large-scale solar energy harvesting, but their ability to recover waste heat is an added benefit.

1.2 | System design

To augment the strengths and mitigate the weaknesses of PV, CSP, and STEG technologies, here we propose a system to achieve efficient solar energy conversion through the integration of photovoltaics, thermoelectric generators, and thermal energy storage fluid (PV-TEG-TES). This system has: direct solar-electrical conversion, inherent energy storage, and high-concentration total solar spectrum utilization, while also capturing PV waste heat, and maintaining PV operational temperatures with reliance on minimal moving parts—only a solar tracker and fluid pump would be required for such a device. Although other hybrid solar energy conversion systems have been proposed and studied such as PV-TEG[16] and PV-TES systems,[17] we present a novel PV-TEG-TES device architecture incorporating state-of-the-art materials.

Figure 1A illustrates the proposed device layer by layer. A single layer photovoltaic solar cell captures incoming visible and ultraviolet light, while the thermal energy storage fluid (TES) and thermoelectric generator capture the infrared component of the solar spectrum, resulting in full solar spectrum utilization by this PV-TEG-TES system. To enhance the temperature difference across the TEG, a thick insulation layer and cooling fluid are designed on opposite sides of the TEG. This arrangement keeps one side hot, and the other cool, increasing TEG electrical generation. Highly thermally conductive 25-μm thick interlayers are located on either side of the TES layer to facilitate cooling of the solar cell and TEG cold side; the TES fluid stores waste heat and maintains the PV at a suitable operating temperature. This stored thermal energy could be used, for example, for dispatchable electricity generation, water desalination, or industrial or domestic process heat.

Systems combining PV and TEG typically place the PV and TEG adjacent to one another such that the hot side of the TEG is in direct contact with the PV, and the TEG is cooled on its side opposite the PV (see Reference 15 for example). This arrangement aims to directly convert PV waste heat to electricity, but limits the temperature difference across the TEG to the difference between the allowable temperature of the solar cell (typically around 100°C maximum) and ambient temperature for a typical temperature difference of—if perfectly cooled—around 80°C across the TEG. This device architecture also loses much heat from the PV and TEG to the environment. In short, the typical arrangement for PV-TEG systems severely limits the performance of the TEG.

To decouple the temperature requirements of the PV and TEG, we propose a novel system architecture with the PV and TEG separated by the TES layer. By putting the

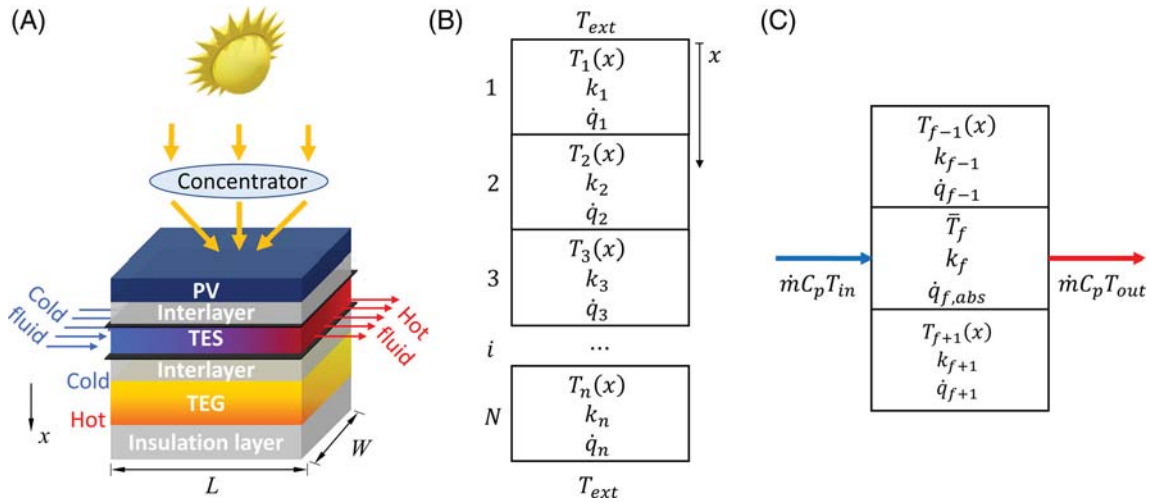

FIGURE 1 Overview of system design and model. (A) Schematic of proposed PV-TEG-TES device. (B) System modeled as 1-D series-connected slabs *1* through *N*, where T_i is the temperature, k_i is the thermal conductivity, and $\dot{q}_i$ is the heat generation rate in layer *i*. (C) Modified system layer at the TES boundary, where solid–fluid thermal transport conditions replace solid slab modeling

TES fluid between the PV and TEG, the TES cools the PV and TEG cold side, taking away and storing waste heat from each. Further, the asymmetry in thermal resistance across the TEG (high heat removal on the TES side of the TEG; high insulation on the hot side) causes the solar absorption and joule heating in the TEG to create a larger temperature gradient across the TEG than in typical PV-TEG systems. Since the PV and TEG are separated by the TES, this configuration allows the cold side of the TEG to go up to the maximum temperature of the PV/fluid temperature, while the hot end of the TEG can rise in temperature as much as is allowed by the TEG materials without concern for degrading PV performance.

1.3 | Modeling motivation

The performance of the system is calculated by analysis of coupled radiative, thermal, fluid, and electrical equations using matrix inversion and a successive over-relaxation technique for convergence.

Because most PV-TEG devices place the TEG in direct conductive contact with the PV, the temperature profile throughout the TEG is not of high importance as the TEG remains much cooler than its melting temperature. However, this PV-TEG-TES device creates a large temperature difference across the TEG to maximize power generation. To this end, we tweak device parameters constrained by TEG melting temperatures, and TES boiling point. Because solar heating and volumetric joule heating exist in our TEG layer, the peak temperature in the TEG actually occurs in the bulk of the device near the "hot side," but not at the "hot side" edge. Our detailed modeling framework allows for predicting the maximum TEG temperature in the bulk of the device, and enables quick parameterized study of material data to assess device performance.

System modeling indicates promising upper bound performance, showing a 1.9% system electrical efficiency conversion gain over solar cells alone, a relative 7.9% improvement. The system can convert and store a total of 79.3% of incident solar energy under a concentration ratio of 673 suns per direct solar spectrum, a concentration chosen to optimize device performance considering optimal TEG operating temperature range and TES boiling temperature.

In short, we present a novel PV-TEG-TES device architecture, showing its viability and performance characteristics. Our detailed modeling framework allows for optimizing device characteristics within constraints of TES boiling temperature and TEG melting temperature.

2 | MULTIPHYSICS MODELING

2.1 | Model overview

In this section, we present our mathematical approach to modeling the complex interacting phenomena in a PV-TEG-TES system. The following subsections describe layer-by-layer the relevant equations, input data, model simplifications, and numerical techniques required to obtain meaningful quantitative performance characteristics of this system. These detailed subsections are included to show exactly what is being modeled, how the device layers interact, and the coupling between different

variables (eg, temperature, TEG electrical current, and internal heat generation).

2.2 | Mathematical approach

A comprehensive modeling framework coupling analytical and numerical modeling techniques is developed for this PV-TEG-TES device to solve heat transfer equations capturing nonlinearly coupled thermal, radiative, fluid, and electrical phenomena for a multi-layer structure, as in Figure 1B, to assess the overall system performance. Each layer is treated with different boundary conditions, heat generation terms, and thermal properties. To retain as much thermal energy as possible, all external sides along the thickness of the system are designed to be thermally insulated. Hence, in-plane temperature gradients are negligible, and the heat transfer model can be simplified to a one-dimensional analysis.

Heat conduction in solids can be described by the thermal diffusion partial differential equation:

$$\rho C_p \frac{\partial T}{\partial t} = \nabla \cdot (k \nabla T) + \dot{q} \tag{1}$$

where ρ is density, C_p is specific heat, T is temperature, t is time, k is thermal conductivity, and $\dot{q}$ is the volumetric heat generation rate.

In one-dimensional steady-state operation with constant properties, the exact solution of the thermal diffusion equation in each layer can be written as:

$$T_i(x) = -\frac{\dot{q}_i}{2k_i}x^2 + C_{i1}x + C_{i2} \tag{2}$$

where i is the layer index, x is the global position coordinate, and C_{i1} and C_{i2} are two unknown constants in each layer determined by boundary conditions.

As Figure 1B shows, the boundary conditions between two neighboring solid layers i and $i+1$ are:

A temperature match condition at each solid-solid layer interface:

$$T_i = T_{i+1} \tag{3}$$

A heat flux match at each solid-solid layer interface:

$$k_i \frac{dT_i}{dx} = k_{i+1} \frac{dT_{i+1}}{dx} \tag{4}$$

At solid-fluid boundaries such as the external device-to-ambient air boundaries, and at internal solid-TES fluid boundaries, the heat flux match condition becomes:

$$\mp k_i \frac{dT_i}{dx} = h\left(T_i - \overline{T}_f\right) \tag{5}$$

where the sign, $\mp$, depends on the whether the interface is solid-to-fluid or fluid-to-solid in the direction of increasing x-coordinate; $\overline{T}_f$ is the average or bulk fluid temperature; and h is the appropriate heat transfer coefficient. For device-to-ambient convection, h is correlated with orientation-dependent Nusselt number, Nu_L, which is a nonlinear function solely of temperature-dependent Rayleigh number, Ra_L:

$$Ra_L = \frac{g\beta}{\nu_f \alpha}(T_s - T_\infty)L^3 \tag{6}$$

where g is the acceleration due to gravity, β is the fluid's coefficient of thermal expansion, ν_f is the fluid's kinematic viscosity, α is the fluid's thermal diffusivity, T_s is the temperature of the surface, T_∞ is the ambient fluid's bulk temperature, and L is the characteristic length, area divided by perimeter. Here we assume a horizontal heated plate geometry, corresponding to the situation where the device is oriented facing exactly upwards towards the sun such that the top and bottom faces are parallel to flat ground. The sun-facing side of the device is modeled as the upper surface of a heated plate; the ground-side face of the device is modeled as the lower surface of a heated plate. Note the nonlinear temperature dependence of Nu_L on Ra_L requires an iterative technique to solve for temperature throughout the device.

For internal solid-fluid boundaries as seen in Figure 1C between the device and internal TES fluid, h is correlated with Nusselt number, Nu_D, and Reynolds number, Re_D:

$$Nu_D = \frac{hD_h}{k_f} \tag{7}$$

$$Re_D = \frac{uD_h}{\nu_f} \tag{8}$$

where k_f is the thermal conductivity of the internal fluid, ν_f is the kinematic viscosity of the fluid, u is the average velocity of the fluid calculated from the mass flow rate $\dot{m}$, and D_h is the hydraulic diameter of the channel, twice the channel thickness. For laminar flow at $Re_D < 2300$, $Nu_D = 7.541$ as calculated for fully-developed flow with constant wall temperature. For turbulent flow at $Re_D > 2300$, a correlation of $Nu_D = f(Re_D)$ is calculated from linear fitting of Burmeister data for fully-developed turbulent flow.[18]

A power balance on the fluid layer with layer index f can be written as:

$$-k_{f+1}A_{f+1}\frac{dT_{f+1}}{dx} = -k_{f-1}A_{f-1}\frac{dT_{f-1}}{dx} + \dot{q}_{f,abs} - \dot{q}_{\text{rem}} \quad (9)$$

where the heat leaving the fluid layer through the fluid-solid boundary with solid layer $f+1$ is equal to what enters the fluid through the solid-fluid boundary with solid layer $f-1$, plus $\dot{q}_{f,\text{abs}}$, the total solar energy absorption rate in the fluid layer (discussed in the Solar Absorption and Heat Generation section) and $\dot{q}_{\text{rem}}$, the total rate of heat removal by the fluid due to advection:

$$\dot{q}_{\text{rem}} = \dot{m}C_p(T_{\text{out}} - T_{\text{in}}) \quad (10)$$

where $\dot{m}$ is the mass flow rate of the fluid, C_p is the specific heat of the fluid, and T_{in} and T_{out} are the average fluid temperatures at the inlet and outlet, respectively.

2.3 | Thermoelectric generator layer

The TEG layer is treated as a solid layer with specialized boundary conditions and heating terms in order to account for the thermoelectric effect and electrical resistive heating. In this model, only the Seebeck Effect and Peltier Effect components of the Thermoelectric Effect are considered; in order to reduce complexity and due to its relatively negligible effect, differential treatment of the Thomson Effect is ignored.

A TEG module (of which the model's TEG 1-D layer comprises many) creates a voltage:

$$V = \pm S_{pn,eff}\left(T_{\text{bot}} - T_{\text{top}}\right) \quad (11)$$

where V is the voltage; $S_{pn,eff}$ is the effective Seebeck coefficient of the module; and T_{top} and T_{bot} are the top and bottom boundary temperatures of the TEG layer. The "effective" Seebeck coefficient is the summation of each TEG PN pellet pair's Seebeck coefficient within a TEG module. The sign, $\pm$, of (11) depends on the PN semiconductor junction orientation of the TEG. To predict an upper limit of efficiency, thermal and electrical contact resistances, as well as convection between TEG pellets, are ignored.

The TEG layer consisting of M modules thermally in parallel and electrically in series then has electrical current, I, of:

$$I = \frac{\text{Total voltage}}{\text{Total resistance}} = \pm\frac{MS_{\text{pn,eff}}\left(T_{\text{bot}} - T_{\text{top}}\right)}{MR_{\text{elec}} + R_{\text{load}}} \quad (12)$$

where M is the number of thermoelectric modules that fill the cross-sectional layer area of the PV-TEG-TES device; R_{elec} is a module's internal electrical resistance; and R_{load} is the load's resistance.

The volumetric heating term in the TEG layer, $\dot{q}_{\text{TEG}}$, includes the volumetric solar absorption term $\dot{q}_{\text{TEG,abs}}$ and electrical resistive heating term as a function of current:

$$\dot{q}_{\text{TEG}} = \dot{q}_{\text{TEG,abs}} + \frac{I^2MR_{\text{elec}}}{A_{\text{TEG}}d_{\text{TEG}}} \quad (13)$$

where A_{TEG} and d_{TEG} are the total cross-sectional area and thickness of the TEG layer, respectively.

The temperature match at the solid-TEG interfaces follows (3). Applying a heat match boundary condition at the solid-TEG boundary, the heat absorption/generation term at each side of the TEG is considered as shown in (14), where again the sign, $\pm$, of the thermoelectric term depends on the device orientation[19]:

$$-k_iA_i\frac{dT_i}{dx} = -k_{i+1}A_{i+1}\frac{dT_{i+1}}{dx} \pm MIS_{\text{pn,eff}}T \quad (14)$$

Note that the area, A, of a solid layer is larger than the area of a TEG module due to gaps between TEG pellets. The TEG's relative decrease in area serves as a thermal concentrator, increasing the temperature difference across the TEG.

The useable electrical power generated by the TEG, P, can be found by:

$$P = MIS_{\text{pn,eff}}\left(T_{\text{bot}} - T_{\text{top}}\right) - I^2R_{\text{elec,tot}} = I^2R_{\text{load}} \quad (15)$$

where $MIS_{\text{pn,eff}}\left(T_{\text{bot}} - T_{\text{top}}\right)$ is the total series TEG voltage times current, minus internal electrical loss, $I^2R_{\text{elec,tot}}$, which gives the power delivered to the load, I^2R_{load}. Note that due to temperature-dependent current, and nonlinearly current-dependent temperature, temperature calculations throughout the device require an iterative approach.

2.4 | Solar absorption and heat generation

To calculate the heat generation term, $\dot{q}_i$, in each layer, the model takes solar spectrum data and a concentration factor by which the sun's radiation is magnified. To ignore the complexities of optics and to estimate an upper limit of efficiency, concentrator losses are ignored (discussed further in the Solar Concentrator and Tracker

section). For this analysis, the standard Air Mass 1.5 Direct Spectrum (AM1.5D) is used as the input solar spectrum for the PV-TEG-TES device, multiplied by a solar concentration factor of 673 to maintain temperatures within optimal TEG operating temperature range, and below TES boiling temperature.

For each layer in the device, a wavelength-dependent spectral absorption coefficient $\alpha_i(\lambda)$ is used. Reflection, scattering, and emission are not considered to eliminate complexity and predict upper bound performance. The remaining spectral intensity of radiation, $I_{\lambda,i}$, immediately after passing through layer i, is given by applying a wavelength-dependent version of Beer's law, where:

$$I_{\lambda,i} = I_{\lambda,i-1} e^{-\alpha_i(\lambda) d_i} \tag{16}$$

where λ is wavelength, and $\alpha_i(\lambda)$ and d_i are the spectral absorption coefficient and thickness of layer i respectively. The calculated spectral intensity remaining after passing through each layer based on the spectral absorption coefficient in Figure 2A is shown in Figure 2B.

The volumetric heat generation term in each layer can then be calculated from how much radiant power a given layer absorbs across all incident wavelengths. The volumetric heat generation term in layer i, $\dot{q}_i$, is calculated as a summation over all wavelengths of: the absorption fraction at each wavelength multiplied by the spectral intensity remaining from the previous layer, $I_{\lambda,i-1}$, multiplied by the spectrum's wavelength data interval, $d\lambda$, multiplied by the layer's area, divided by the layer's volume, where d_i is the layer thickness. Stated as an equation, the volumetric heat generation term in layer i is:

$$\dot{q}_i = \frac{1}{d_i} \sum_{\lambda} \left(1 - e^{-\alpha_i(\lambda) d_i}\right) I_{\lambda,i-1} d\lambda \tag{17}$$

2.5 | PV layer solar absorption

The device design uses a sufficiently thick PV layer such that all in-band light is absorbed. The PV layer absorption calculation uses the PV layer's bandgap as an energy cutoff, whereby all incident photons with energy at or above the bandgap are absorbed. For each photon absorbed, energy equal to the bandgap is converted to electricity and all excess absorbed energy is converted to heat as a model of photon thermalization. Any photons with energy below the PV bandgap are transmitted to the next layer. In our modeling, an energy loss factor of 46.1% is used based on the typical performance of a GaAs PV module, capturing efficiency loss due to electron-hole recombination, internal resistive losses, and further electrical loss.[1] Because the PV is the first layer in the device, it behaves optically as an independent PV module would. Thus, the inclusion of this loss factor allows for comparing the PV-TEG-TES device as a whole to an independent PV module with equal performance.

2.6 | Solar concentrator and tracker

An energy conversion device relying on high heat fluxes produced by focused sunlight requires concentrating optics and dual-axis sun tracking to ensure capturing the maximum heat flux for maximum power production and efficiency. Concentrating optics may take the form of mirrors or lenses, and the tracker options are varied. These optical concentrators and trackers are inherently

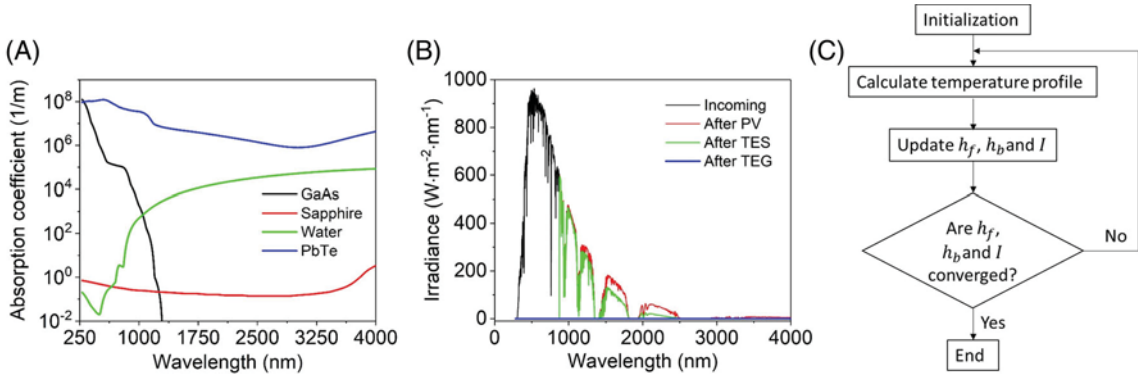

FIGURE 2 Model input and algorithm. (A) Spectral absorption coefficient of different materials. (B) Remaining solar spectrum after transmitting through different layers, indicating utilization of the full solar spectrum. (C) Flow chart of the iteration framework

three-dimensional, and result in spatially-varying illumination and heating both by design and due to optical aberrations (concentrators typically produce an illumination profile diminishing from a central focal point).

However, due to the complex nature of interacting heat conduction, convection, radiation, and electrical and fluid flow phenomena present in a PV-TEG-TES device, and considering the sides of such a device would be insulated to mitigate heat loss (eliminating temperature gradients in two dimensions), our paper models these phenomena with a one-dimensional approach, allowing for detailed parametric analysis.

A one-dimensional factor mimicking losses due to three-dimensional optics could theoretically be included for this PV-TEG-TES model but any efficiency losses it creates could merely be cancelled out by increasing its concentration factor. One could also include spectral absorption losses in the optical concentrator, but these details would be minor compared to the effects of fully modeling the concentrator with three-dimensional ray tracing, requiring a three-dimensional heat transfer model as well.

Likewise, while the power consumption of the required motors and programmable logic controllers for dual-axis solar tracking could be a significant percentage of overall device power generation for non-concentrating photovoltaics, this percentage of generated power would be divided by roughly the solar concentration factor and is thus considered negligible for our highly-concentrating system.

Concentrator-induced spatially-varying illumination in photovoltaics could alter device performance as more highly illuminated areas of the cells will generate more power. To mitigate performance loss, photovoltaic layers could be broken up into smaller cells and wired together to match current or voltage of other similarly illuminated cells. While our device model does not account for spatially-varying illumination, it should be noted that our one-dimensional concentration factor would be the average concentration of two-dimensional spatially-varying illumination.

Considering all the above factors, for our detailed one-dimensional model which allows for exploring device parameters, optics and tracking are considered outside the scope of this paper.

Further, one of the simplifying assumptions of our one-dimensional modeling approach is that solar absorption and joule heating are uniform throughout the volume of the TEG, allowing a temperature gradient to form in the TEG due to thermal resistance asymmetry (low thermal resistance at the cold side, high thermal resistance at the hot side). This temperature gradient could be enhanced by using optics to direct solar radiation further towards the hot side of the TEG for absorption, which would lead to a larger temperature difference across the TEG, improving overall device performance. As a result, we consider our assumption of uniform volumetric heating in the TEG a slightly conservative assumption.

2.7 | Iterative solution

Despite the linear nature of conduction heat transfer and the generally linear framework of this simulation, due to the nonlinear temperature-dependent external heat transfer coefficients, and nonlinear coupling between temperature and electrical current in the TEG layer, the governing equations of this system must be solved via iterative technique as illustrated in Figure 2C. The boundary conditions (3), (4), (5), (9), (10), and (14), along with supplemental equations for heat transfer coefficients represent $2N$ equations for the $2N$ coefficients C_{i1} and C_{i2} in (2) for N device layers. Once the coefficients are determined, the exact solution for the temperature distribution in each layer is given by (2). This model uses matrix inversion with a successive overrelaxation technique to solve for the coefficients and ensure solution convergence. While solving for TEG electrical current using the successive overrelaxation technique, a residual r is defined as the difference between the directly calculated current per (12), $\overline{I_{\text{new}}}$, and the previous iteration's calculated current, I_{old}:

$$r = \overline{I_{\text{new}}} - I_{\text{old}} \tag{18}$$

The new current used for the next iteration's temperature calculations, I_{new}, is then calculated as:

$$I_{\text{new}} = I_{\text{old}} + wr = (1-w)I_{\text{old}} + w\overline{I_{\text{new}}} \tag{19}$$

where w is a weighting factor applied to the residual. A residual weighting of 0.001 is used to avoid solution instability caused by electrical current changing significantly each iteration and to ensure solution convergence. Solution convergence is defined by heat transfer coefficients changing by no more than 0.01% per iteration, and TEG electrical current changing by no more than 10^{-5}% per iteration (discussed further in the Error Tolerance and Analysis section).

2.8 | Material selection

The proposed device materials are shown in Table 1. To best assess an upward bound of performance for the proposed PV-TEG-TES system, state of the art materials are

TABLE 1 Material properties and model inputs

Layer material	PV (GaAs), Interlayer 1 (Sapphire), Internal Fluid (Water), Interlayer 2 (Sapphire), TEG (PbTe/SnSe), Insulation layer (Silica aerogel)
Layer thicknesses	0.5, 0.025, 0.05, 0.025, 3, 75 mm
Thermal conductivities	52, 27, 0.596, 27, 0.725, 0.01 W/(m·K)
Device width and length	10 cm
PV bandgap	1.42 eV
PV loss factor	46.1%
TEG fill factor (A_{TEG}/A_{Total})	0.44
TEG Seebeck coefficient per pellet pair	7.3×10^{-4} V/K
TEG electrical resistivity	2.7×10^{-4} Ω·m
TEG load resistance	195 Ω
Fluid inlet temperature	20°C
Mass flow rate	1.02×10^{-2} kg/s
Fluid specific heat	3.993 kJ/(kg·K)
Solar concentration	673 Suns
Solar spectrum	AM1.5D (Direct normal irradiance)

considered without concern for their associated costs. In Table 1, the thickness of each layer, fluid mass flow rate, and optimal TEG loading is optimized by parameter sweeping, which is discussed in the Final Design section.

2.9 | Photovoltaic module

The photovoltaic module is the primary driver of electrical energy conversion in the device, and therefore its goal is to convert the largest portion of the solar spectrum into electricity as possible without otherwise reducing device performance. For single-junction photovoltaic cells operating under the AM1.5 solar spectrum, there exists a theoretical maximum efficiency known as the Shockley-Queisser limit,[20] found by performing a detailed balance analysis on a single-junction photovoltaic cell. For an ideal solar cell, this maximum efficiency is approximately 33.7%, and occurs for a photovoltaic cell with a bandgap of 1.34 eV. Thus, to maximize efficiency for our device, we chose a type of photovoltaic cell with a bandgap close to this Shockley-Queisser limit, that is, GaAs with a bandgap of 1.42 eV.

The selection of photovoltaic material/bandgap is a choice between absorbing more solar radiation, and absorbing less solar radiation but doing so more efficiently. That is, a lower bandgap photovoltaic absorbs more sunlight (more photons with energy at or above its lower bandgap are absorbed), but absorbs sunlight less efficiently (photons with energy above its bandgap have their excess energy converted to heat). In contrast, a higher bandgap photovoltaic absorbs less sunlight (more photons with energy below its higher bandgap are transmitted), but absorbed photons are converted to electricity more efficiently (there is less excess photon energy above the bandgap to convert to heat). In our choice of GaAs we seek to maximize efficiency by finding the balance between these competing phenomena.

Likewise, our device could have used a more ubiquitous silicon photovoltaic cell, which has a lower bandgap than GaAs (silicon: 1.12 eV), meaning it would absorb more solar radiation, but it would also convert more of the absorbed energy directly into heat. Our device does collect heat, however, a lower bandgap cell would lose some of this heat directly to the environment, and limit the amount of solar radiation that reaches the TEG. Overall, a lower bandgap PV limits the total conversion efficiency of this device, so we have chosen GaAs.

Also, note that GaAs transmits much solar radiation (photons with energy below its bandgap) that would be wasted in an individual photovoltaic device. However, in a PV-TEG-TES system, this transmitted energy is captured by the TES and TEG layers, adding to the overall device heat absorption/efficiency, mitigating photovoltaic transmission losses, and allowing for high absorption across the solar spectrum.

Our specific choice of a GaAs module is based on a world record GaAs single junction device made by Alta Devices at 28.8% efficiency for the cells, which reduces to 24.1% efficiency for the module as a whole.[1,2] With a bandgap of 1.42 eV near the Shockley-Queisser limit, our chosen GaAs module transmits primarily infrared radiation.

2.10 | Thermoelectric generator modules

Informed by the results of the predicted temperatures experienced across the TEG, the TEG itself is made of P-type hierarchically structured and doped bulk scaled PbTe with SrTe,[21] and N-type SnSe,[22] which represent state of the art materials for a mid-grade temperature regime,[23] able to operate within a range of 750 to 900 K with a figure of merit, ZT, greater than 2. These TEG semiconductors are expected to absorb the majority of any radiation remaining after the photovoltaic layer. Since this modeling framework is one-dimensional, the TEG layer uses only one material's absorption data, that of PbTe.[24] In optimizing the system for maximum temperature difference across the TEG, the melting temperature of the thermoelectric materials is also a key parameter informing material selection.

2.11 | Thermal energy storage fluid

Our choice of water for the TES fluid is due to its relatively low absorption of the visible and near infrared spectrums through a thin channel (allowing solar energy to reach the TEG), its ubiquity (allowing for broad application and low cost), compatibility with common pumps, sufficiently high thermal conductivity, and sufficiently high boiling point (100°C, high enough to permit high solar concentrations, and close to typical maximum operating temperatures of PV cells). Our choice of water performs as needed without limitation; it does not add concerns for costs, chemical handling, specialized pumps/equipment, or other constraints that may come with more exotic fluids. In short, water meets all performance requirements with virtually no drawbacks. We found little need to investigate other fluids for this application.

2.12 | Interlayers and insulation layers

After the PV cell, a sapphire interlayer is chosen for its high thermal conductivity and relative transparency to infrared radiation. The next interlayer is also made of sapphire for similar reasons as stated before, such that the sapphire maintains the cold temperature side of the TEG. Finally, the insulation layer is selected as ultralow thermal conductivity (0.01 W/m/K) silica aerogel[25] to maximize the temperature difference across the TEG and retain heat within the device, thus boosting TEG electrical generation.

3 | RESULTS AND DISCUSSION

3.1 | Parametric sweeps and structure optimization

The device configuration proposed is shown in Figure 1A and discussed in the System Design section of this paper. This device layer configuration allows for utilization of the entire solar spectrum, maintaining PV cells at suitable working temperature and creating a temperature gradient across the TEG. To maximize solar spectrum utilization, device efficiency, and to ensure adequate PV cooling, parametric sweeps are carried out for some device parameters including: the thickness of TES-TEG interlayer and insulation layer, TES channel thickness, solar concentration factor, TES mass flow rate, and the load resistance of the TEG. These parametric sweeps display trends for optimization, however they must be used with constraints such as: TES outlet temperature must remain below its boiling point; layer thicknesses must remain within realizable and practical limits; pumping power required must remain a small fraction of electrical generation; and TEG temperatures must remain in optimal performance range and below melting temperatures. Table 1 gives the key parameters of our design after optimization considering these restrictions.

The system electrical generation efficiency (defined as total electrical power generated divided by total incident solar power) is plotted vs load resistance and mass flow rate in Figure 3A. This surface plot shows a clear optimal load resistance around 195 Ohms, which is further used to evaluate upper bound device performance. Note that this calculated optimal load resistance may differ from that calculated by the maximum power transfer theorem due to a portion of the TEG's internal heat generation contributing to the temperature gradient across the TEG and to heating the TES. Further, while in real resistive load scenarios the load resistance is not adjustable, because this PV-TEG-TES device comprises many individual TEG pellet pairs, these could be divided and wired to achieve application-appropriate voltage.

Figure 3A shows that TES mass flow rate has little effect on the overall electrical performance of the device when the mass flow rate is nonzero. This realization provides two pieces of further insight: (a) changing the mass flow rate of the TES fluid in this configuration likely cannot control the thermal energy storage vs electrical energy conversion rates; and (b) since the TES fluid flow rate has little effect on the overall device performance, the flow rate in this layer can instead be used to control the desired outlet temperature of the fluid for either process heat or further electrical power generation. For

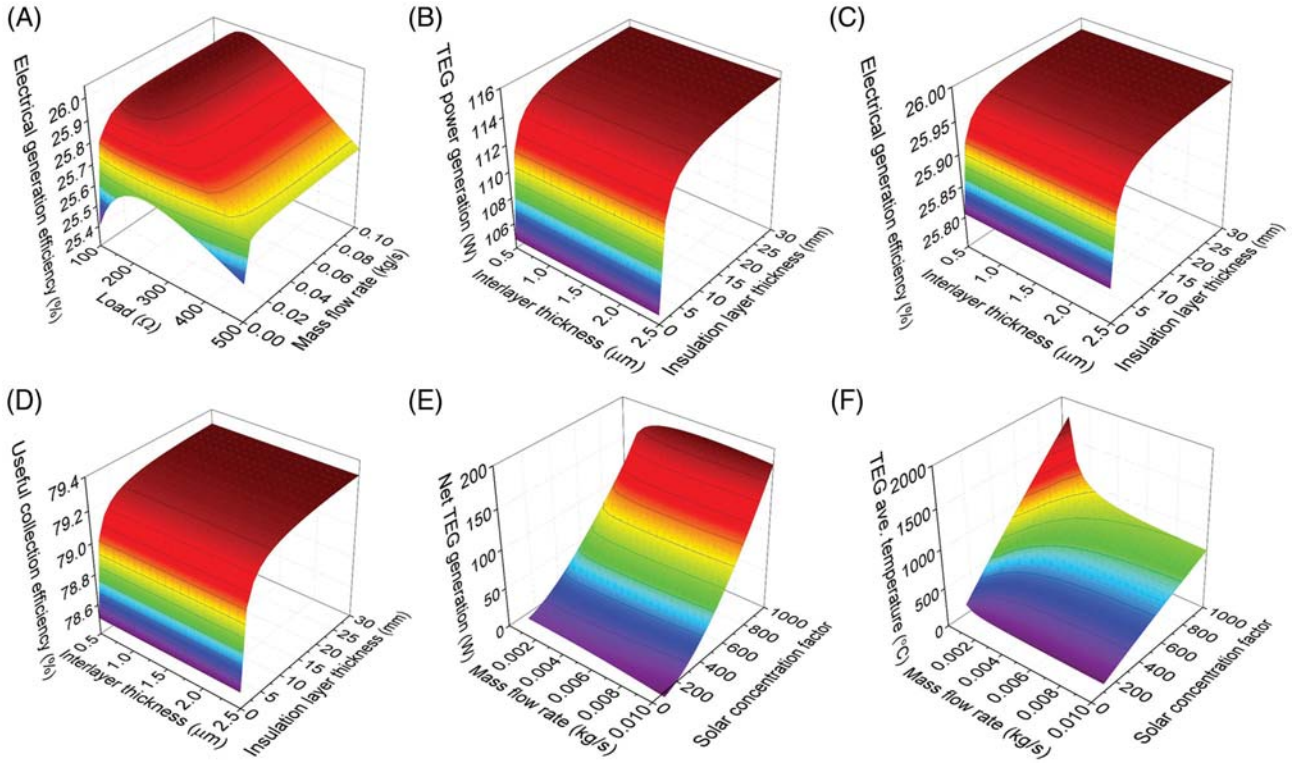

FIGURE 3 Parametric analysis and optimization of PV-TEG-TES system. (A) Surface plot of the system electrical generation efficiency vs TES mass flow rate and load resistance. (B) Surface plot of TEG power generation rate vs the thickness of the interlayers and the insulation layer. (C) Surface plot of the system electrical generation efficiency vs the thickness of the interlayers and the insulation layer. (D) Surface plot of the useful collection efficiency vs the thickness of the interlayers and the insulation layer. (E) Surface plot of net TEG power generation rate vs TES mass flow rate and solar concentration. (F) Surface plot of TEG average temperature vs TES mass flow rate and solar concentration

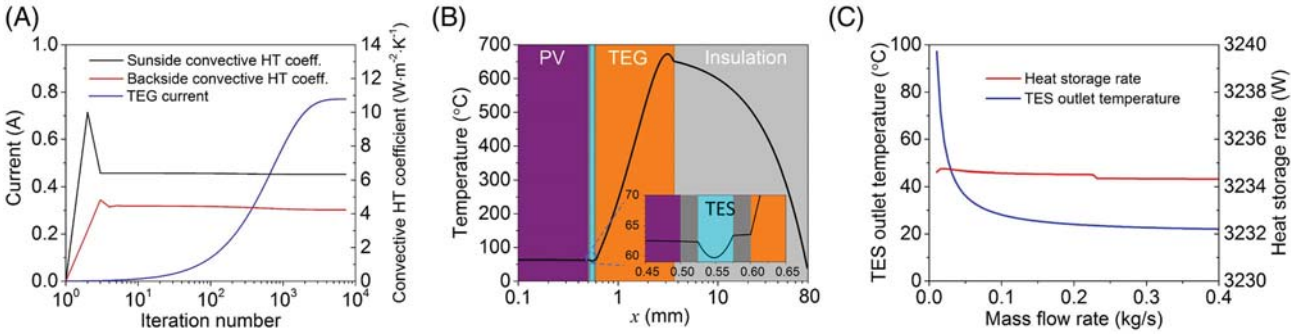

FIGURE 4 Simulation results for optimized final design. (A) Convergence of algorithm for current through TEG and convective heat transfer coefficients. (B) Temperature within the device as a function of the global layer thickness coordinate. (C) TES outlet temperature and heat storage rate vs TES mass flow rate

further electrical generation, the highest temperature up to boiling point is desired for maximum thermodynamic efficiency, but temperature may be controlled to lower temperature for specific domestic or industrial application without affecting the overall performance of the device. Since the total heat transfer into the fluid is roughly the same regardless of mass flow rate, the temperature difference between the inlet and outlet temperature varies inversely with the mass flow rate, as in (8). Figure 4C illustrates these expected behaviors: TES outlet temperature varies inversely with mass flow rate, and mass flow rate only marginally affects heat storage rate,

even considering transition to turbulence at a mass flow rate value of around 0.25 kg/s.

Decreasing the thickness of the TES layer results in less solar energy absorption in the TES layer and more in the TEG layer thus increasing power generation in the TEG. However, while the TES outlet temperature can be controlled by the mass flow rate, the TES layer parameters must be chosen such that: the TES remains below its boiling point (100°C); the TEG temperature remains within optimal range and below its melting point; and the pumping power required remains a small fraction of generated electricity. As a rough order of magnitude approximation, the pumping power per unit width P'_{pump} required for fully-developed laminar flow in a two-dimensional channel is:

$$P'_{\text{pump}} = \frac{96\dot{m}'^2\mu L}{\eta\rho^2 D_H^3} \tag{20}$$

where $\dot{m}'$ is mass flow rate per unit width W (see Figure 1A); μ is the fluid's dynamic viscosity; L is the length of the channel in the direction of flow; η is the electrical-mechanical efficiency of the pump; ρ is the fluid's density; and D_H is the hydraulic diameter of the channel, twice the channel's thickness. Thus, a factor of 10 reduction in the TES layer thickness results in a factor of 1000 increase in pumping power, all else equal. Likewise, a reduction in TES layer thickness increases TEG temperatures, which must be mitigated by increasing mass flow rate, further multiplying required pumping power. Due to these constraints, the performance of the TEG cannot achieve otherwise optimal performance, that is, the TEG could perform better in this configuration, but at the detriment of the system as a whole. In Figure 3E, the difference between TEG power generation and pumping power is plotted vs solar concentration factor and TES mass flow rate. This plot shows that for larger values of mass flow rate, due to increased pumping power, the net energy generation of the TEG and pump decreases and eventually becomes negative. Figure 3F shows the TEG average temperature vs solar concentration and TES mass flow rate. Note that for optimal and safe operation (with maximum TEG temperatures sufficiently below its melting point) the TEG average temperature must remain around 500°C. Thus, the results of Figure 3E,F show a fairly narrow range of acceptable solar concentration factors and mass flow rates. However, they also show that at a set solar concentration, with a mass flow rate greater than 0.001 kg/s, the mass flow rate has negligible effect on the net TEG-pump power generation, confirming that the mass flow rate can be used exclusively as a control for TES outlet temperature. This control may be useful for supplying heat for different processes, or keeping the TES outlet temperature under boiling point given transient environmental conditions.

Figure 3D shows how the useful collection efficiency (defined as the total electrical and thermal energy conversion rates divided by total incident solar energy rate) changes vs the thickness of TES-TEG interlayer and insulation layers. Figure 3D indicates that the useful collection efficiency can be enhanced by a thick insulation layer, but remains almost entirely independent of the thickness of the TES-TEG interlayer. These relationships indicate that the system performance can be enhanced both electrically and thermally by structure optimization.

The surface plots in Figure 3B,C show system electrical generation efficiency and TEG power generation rate vs the thickness of the TES-TEG interlayer and insulation layers, respectively. The TES-TEG interlayer and insulation layers are on either side of the TEG as seen in Figure 1. The performance of the TEG can be tuned by changing the thickness of the TES-TEG interlayer and insulation layers. From Figure 3B,C, a thin TES-TEG interlayer and a thick insulation layer benefit both the TEG power generation and the system electrical generation efficiency with the same trends. A thin TES-TEG interlayer can enhance the heat exchange between fluid and the cold side of the TEG, such that the cold side of the TEG is maintained at a relatively low temperature. A thick insulation layer can retain the heat inside the system overall, and in doing so also boost the temperature of the hot side of the TEG layer. These effects combined produce a greater temperature difference across the TEG, resulting in greater electrical generation. In this system, as can be seen from Figure 3B,C, increasing the TEG power generation simultaneously increases the system electrical generation efficiency, meaning the overall device electrical performance increases with increasing TEG performance. If the opposite were true, it would indicate the incorporation of the TEG hurts the solar energy harvesting capability of the device overall, likely invalidating this layer configuration and perhaps the viability of a PV-TEG-TES system entirely. These results thus validate the proposed device layout, offering promise for increased PV-TEG-TES device performance with improved materials.

3.2 | Final design and performance

The optimized parameters in Table 1 are used for our final calculation of upper bound performance for this PV-TEG-TES device, the solution of which converges (ie, heat transfer coefficients change <0.01% and TEG

electrical current changes $<10^{-5}$% per iteration) after roughly 7000 iterations, as shown in Figure 4A. The top and bottom heat transfer coefficients converge far more quickly than the TEG electrical current, indicating the primary difficulty in convergence stems from the electrical current.

Figure 4B shows the temperature profile throughout such a device. The temperature of the PV solar cell is maintained below 65°C, well within the range of suitable working temperatures. A large temperature gradient is generated in the TEG, which boosts the power generation from the thermoelectric effect, while its average temperature is kept at 500°C, and its maximum temperature kept below 673°C, well below the melting temperature of the TEG materials. The temperature decreases from 650°C to near room temperature in the silica aerogel insulation layer, which demonstrates good thermal insulation at the bottom of the PV-TEG-TES device.

As seen in Figure 2B, in the PV layer most visible and ultraviolet light is absorbed. In the TES, only a small portion of remaining light in the infrared range is absorbed, leaving the TEG to absorb much of the PV-transparent radiation. The radiation energy remaining after the TEG layer is virtually zero, as shown in Figure 2B, indicating the device absorbs nearly all the incoming solar radiation, using the entire solar spectrum as intended.

The simulation of this device/configuration yields the key performance metrics given in Table 2. Note that because the PV is the first layer in the device, its performance is roughly identical to PV performance without the rest of the PV-TEG-TES system, provided it is kept sufficiently cool, and under identical illumination conditions. Note that the electrical efficiency here is found merely by adding the PV and TEG power outputs divided by the total incident solar energy rate. Thus, since the overall electrical efficiency is 26.0% and the PV efficiency alone is 24.1%, including the TEG increases the electrical efficiency by approximately 1.9 percentage points (a relative 7.9% improvement). Further, the overall useful collection efficiency (electrical power generation plus thermal energy storage rates divided by total incident solar energy rate) is approximately 79.3%, leading to overall calculated system losses (losses due to assumed internal and electrical PV losses, and due to heat transfer to the external environment) around 20.7%, far less than those of conventional PV technologies. Note that although electrical joule heating in the TEG could be considered electrical loss, due to the TEG's position between the TES and insulation layers, this heat generation can instead add to the TEG temperature gradient and to TES energy storage. In addition, with these device parameters, the PV-TEG-TES device requires pumping power only on the order of 10 W, and increases the working fluid temperature to 99°C, near the limit of its boiling point and maximum internal energy in the liquid state.

TABLE 2 Key performance metrics of PV-TEG-TES system

Photovoltaic electrical power generation	1.46 kW
TEG electrical voltage	150 V
TEG electrical current	0.77 A
TEG electrical power generation	115.7 W
System electrical power generation (PV + TEG)	1.58 kW
TES fluid heat storage rate	3.23 kW
System electrical generation efficiency (PV + TEG)	26.0%
Useful collection efficiency (Heat + Electrical)	79.3%

3.3 | Error tolerance and analysis

The two most challenging aspects of convergence for our PV-TEG-TES model are the heat transfer coefficients at the device-ambient interfaces and the TEG current as they are nonlinear and depend on temperature. These coefficients determine the temperature profile throughout the device, which is based on analytical formulas for energy conservation, that is, if these terms converge, our analytical model should be consistent with physical principals. The tolerance for these coefficients and TEG current were determined via trial-and-error to ensure model convergence.

This trial-and-error for tolerance values ensures our model is converged in terms of changing model output, and we also confirm this convergence is consistent with physical quantities. At a high level, our model of the PV-TEG-TES system models energy/power balances across various phenomena in the device. So, to rigorously validate the sufficiency of these convergence criteria, a check of input vs output power is also performed.

The total device power consumption (solar power converted to electricity, stored as heat, or lost to the environment) is calculated as 6063.6 W. Compared to the model's solar energy input for a 10 cm by 10 cm device at 673 suns with a total input power of 6058.1 W, this gives a miniscule total model power error of 0.09%, indicating sufficient convergence.

The cause of this miniscule power discrepancy is likely due in part to the way solar spectrum data are processed to match our model's absorption data, that is, solar spectrum data and layer absorption coefficient data are interpolated by our model such that each has a data point at every wavelength present across all datasets. The interpolation of solar spectrum data and layer absorption data to every wavelength inserts some error into how

TABLE 3 Model power accounting and error analysis

Component	Power (W)
PV electrical generation	1460.0
PV module/environmental losses	1253.2
TEG electrical generation	115.7
TES heat storage	3234.6
Summation	**Power (W)**
Total device power consumption	6063.6
Total model solar input	6058.1
Device model error	0.09%
Solar power (Left Riemann sum)	6062.4
Solar power (Right Riemann sum)	6054.3
Solar power (integration error)	0.13%

much energy exists in the solar spectrum at certain wavelengths.

With the error analysis described above, we have verified both convergences, and that convergence is consistent with energy conservation. Another worthy analysis is comparing this "error" to the error in the model's raw energy input data to verify that what appears to be an insignificant error of 0.09% is indeed insignificant. Integrating raw solar spectrum data over wavelength, and multiplying by device area (10 cm by 10 cm) and solar concentration factor (673 suns) gives the total input solar power. However, depending on the numerical integration technique used, the total input power differs slightly. As a simple example, using a Left Riemann Sum approach gives a total input power of 6062.4 W, whereas a Right Riemann Sum approach gives a total input power of 6054.3 W, giving an error between these numerical techniques of 0.13%.

In short, our model gives an energy error of 0.09%, which is less than the uncertainty in numerical techniques due to using the solar spectrum power data itself—our model gives virtually as low of an error as possible with AM1.5D spectrum data. See Table 3 for a full accounting of power.

4 | CONCLUSION AND FUTURE WORK

This paper presents an integrated PV-TEG-TES solar energy conversion system with novel device architecture featuring direct solar-electrical conversion, waste heat harvesting, and inherent energy storage, augmenting the strengths, and mitigating the weaknesses of conventional solar energy harvesting technologies. Through a multiphysics radiative, thermal, fluid, and electrical analysis, the system has been shown to have a direct electrical efficiency of up to 26.0%, a 1.9 percentage point gain over a conventional GaAs PV module (ie, a relative efficiency improvement of 7.9%). In addition, the system has been shown to be able to capture 53.3% of incident solar energy as heat, which could be converted to electricity with a heat engine and dispatched as desired, or used as industrial or domestic process heat. The electrical and stored energy efficiencies added together form a useful energy collection efficiency of 79.3%, resulting in an overall incident solar energy loss of 20.7%, far less than conventional PV systems.

Though simplified in nature, due to the highly coupled multiphysics interactions present in a PV-TEG-TES device, the insights gathered from this analysis can provide a starting point for designing a practical three-dimensional PV-TEG-TES system. This one-dimensional analysis framework provides initial guidance for selecting viable solar concentration, materials, fluid flow parameters, and device layer order and thicknesses, parameters difficult and computationally intensive to arrive at solely with a full three-dimensional modeling framework. An expansion to full three-dimensional system modeling would benefit in performance prediction accuracy from: optical design (which may allow for greater TEG performance with directed heating); radiative reemission, reflection, and scattering; full three-dimensional fluid flow; and incorporation of spatially/temperature-dependent TEG material properties.

Future research into PV-TEG-TES systems could expand on this study by determining the best specific applications for such a device (eg, residential, industrial or utility implementation, and geographic feasibility) via investigating: electrical grid implementation and related circuity, LCOE economic analysis ($/kWh) including the effects of system degradation (eg, cooling channel fouling affecting required pumping power, and TEG absorption), and ultimately three-dimensional design, fabrication, and device performance testing.

DATA AVAILABILITY STATEMENT

The data that support the findings of this study are available from the corresponding author upon reasonable request.

ORCID

Nicholas Farrar-Foley https://orcid.org/0000-0002-5769-9719
Nicolas Augustus Rongione https://orcid.org/0000-0002-9895-1896
Adrienne S. Lavine https://orcid.org/0000-0002-5580-7608
Yongjie Hu https://orcid.org/0000-0001-7225-1130

REFERENCES

1. Green MA, Emery K, Hishikawa Y, Warta W, Dunlop ED, Levi DH, Ho-Baillie AWY. Solar cell efficiency tables (version 49). *Prog Photovoltaics Res App*. 2017;25(1):3-13.
2. *Best Research-Cell Efficiency Chart*. Golden, CO: National Renewable Energy Laboratory; 2019.
3. Philibert C, Frankl P, Tam C. *Technology Roadmap: Solar Photovoltaic Energy*. Paris, France: International Energy Agency; 2014.
4. Aboelwafa O, Fateen S-EK, Soliman A, Ismail IM. A review on solar rankine cycles: working fluids, applications, and cycle modifications. *Renew Sustain Energy Rev*. 2018;81(1): 868-885.
5. Fuqiang W, Ziming C, Jianyu T, Yuan Y, Yong S, Linhua L. Progress in concentrated solar power technology with parabolic trough collector system: a comprehensive review. *Renew Sustain Energy Rev*. 2017;79:1314-1328.
6. Y. Ma, X. Zhang, M. Liu, J. Yan, J. Liu, "Proposal and assessment of a novel supercritical CO_2 Brayton cycle integrated with LiBr absorption chiller for concentrated solar power applications," *Energy*, vol. 148, pp. 839–854, Apr. 2018.
7. Modi A, Bühler F, Andreasen JG, Haglind F. A review of solar energy based heat and power generation systems. *Renew Sustain Energy Rev*. 2017;67:1047-1064.
8. Philibert C, Frankl P, Dobrotkova Z. *Technology Roadmap: Concentrating Solar Power*. Paris, France: International Energy Agency; 2010.
9. Dresselhaus MS, Chen G, Tang MY, et al. New directions for low-dimensional thermoelectric materials. *Adv Mater*. 2007; 19(8):1043-1053.
10. Zebarjadi M, Esfarjani K, Dresselhaus M, Ren Z, Chen G. Perspectives on thermoelectrics: from fundamentals to device applications. *Energy Environ Sci*. 2012;5(1):5147-5162.
11. He J, Tritt TM. Advances in thermoelectric materials research: looking back and moving forward. *Science*. 2017;357(6358): 1369-1379.
12. Shi X-L, Zou J, Chen Z-G. Advanced thermoelectric design: from materials and structures to devices. *Chem Rev*. 2020; 120(15):7399-7515.
13. Attivissimo F, Nisio AD, Lanzolla AML, Paul M. Feasibility of a photovoltaic-thermoelectric generator: performance analysis and simulation results. *IEEE Trans Instrum Meas*. 2015;64(5): 1158-1169.
14. Sundarraj P, Maity D, Roy SS, Taylor RA. Recent advances in thermoelectric materials and solar thermoelectric generators - a critical review. *RSC Adv*. 2014;4(87):46860-46874.
15. Rezania A, Rosendahl LA. Feasibility and parametric evaluation of hybrid concentrated photovoltaic-thermoelectric system. *Appl Energy*. 2017;187:380-390.
16. Aljibory MW, Hashim HT, Abbas WN. A review of solar energy harvesting utilising a photovoltaic–thermoelectric integrated hybrid system. *IOP Conference Series: Materials Science and Engineering*. 2021;1067(1):1-16.
17. Xu Q, Ji Y, Riggs B, et al. A transmissive, spectrum-splitting concentrating photovoltaic module for hybrid photovoltaic-solar thermal energy conversion. *Sol Energy*. 2016;137:585-593.
18. Burmeister LC. *Convective Heat Transfer*. 2nd ed. Hoboken, NJ: John Wiley & Sons; 1993:338-342.
19. Bergman TL, Lavine AS, Incropera FP, DeWitt DP. *Fundamentals of Heat and Mass Transfer*. 7th ed. Hoboken, NJ: John Wiley & Sons; 2011:182-187.
20. Shockley W, Queisser HJ. Detailed balance limit of efficiency of p-n junction solar cells. *J Appl Phys*. 1961;32(3):510-519.
21. Biswas K, He J, Blum ID, et al. High-performance bulk thermoelectrics with all-scale hierarchical architectures. *Nature*. 2012; 489:414-418.
22. Chang C, Wu M, He D, et al. 3D charge and 2D phonon transports leading to high out-of-plane ZT in n-type SnSe crystals. *Science*. 2018;360(6390):778-783.
23. Zhu T, Liu Y, Fu C, Heremans J, Snyder J, Zhao X. Compromise and synergy in high-efficiency thermoelectric materials. *Adv Mater*. 2017;29(30):1605884.
24. Ekuma CE, Singh DJ, Moreno J, Jarrell M. Optical properties of PbTe and PbSe. *Phys Rev B*. 2012;85(8):085205.
25. Hartmann J. *Thermal and Solar Optical Properties of Silica Aerogel*. Lawrence Berkeley Laboratory, Berkeley, CA: Windows and Daylighting Group; 1986.

How to cite this article: Farrar-Foley N, Rongione NA, Wu H, Lavine AS, Hu Y. Total solar spectrum energy converter with integrated photovoltaics, thermoelectrics, and thermal energy storage: System modeling and design. *Int J Energy Res*. 2022;46(5):5731-5744. doi:10.1002/er.7518